PNAS
www.pnas.org

Supplementary Information for

Symmetric activation and modulation of the human calcium-sensing receptor

Jinseo Park[a,1], Hao Zuo[a,1], Aurel Frangaj[a,1], Ziao Fu[b,1], Laura Y. Yen[c,1], Zhening Zhang[b,1], Lidia Mosyak[a], Vesna N. Slavkovich[d], Jonathan Liu[a], Kimberly M. Ray[a], Baohua Cao[a], Francesca Vallese[e,f], Yong Geng[a], Shaoxia Chen[g], Robert Grassucci[b], Venkata P. Dandey[c], Yong Zi Tan[c,h,i,j], Edward Eng[c], Yeji Lee[a], Brian Kloss[k], Zheng Liu[b], Wayne A. Hendrickson[b,h,k,2], Clinton S. Potter[b,c], Bridget Carragher[b,c], Joseph Graziano[d], Arthur D. Conigrave[l,2], Joachim Frank[b,m,2], Oliver B. Clarke[e,f,h,2], Qing R. Fan[a,n,2]

[a]Department of Pharmacology, Columbia University, New York, NY 10032;
[b]Department of Biochemistry and Molecular Biophysics, Columbia University, New York, NY10032;
[c]National Resource for Automated Molecular Microscopy, Simons Electron Microscopy Center, New York Structural Biology Center, New York, NY 10027;
[d]Department of Environmental Health Sciences, Columbia University, New York, NY 10032;
[e]Department of Anesthesiology, Columbia University, New York, NY 10032;
[f]Irving Institute for Clinical and Translational Research, Columbia University, New York, NY 10032;
[g]Medical Research Council Laboratory of Molecular Biology, Cambridge CB2 0QH, UK.
[h]Department of Physiology and Cellular Biophysics, Columbia University, New York, NY 10032;
[i]Department of Biological Sciences, National University of Singapore 119077, Singapore;
[j]Disease Intervention Technology Laboratory, Agency for Science, Technology and Research (A*STAR) 119077, Singapore;
[k]Center on Membrane Protein Production and Analysis, New York Structural Biology Center, New York, NY 10027;
[l]School of Life & Environmental Sciences, Charles Perkins Centre, University of Sydney, Camperdown, NSW 2006, Australia;
[m]Department of Biological Sciences, Columbia University, New York, NY 10027;
[n]Department of Pathology and Cell Biology, Columbia University, New York, NY 10032

[1]These authors contributed equally to this work.
[2]To whom correspondence should be addressed. W.A.H., A.D.C., J.F., O.B.C., Q.R.F.
Email: wah2@cumc.columbia.edu; arthur.conigrave@sydney.edu.au; jf2192@cumc.columbia.edu; oc2188@cumc.columbia.edu; qf13@cumc.columbia.edu.

This PDF file includes:

Extended Materials and Methods
Figures S1 to S10
Tables S1 to S2
Legends for Movies S1 to S2
SI References

Other supplementary materials for this manuscript include the following:

Movies S1 to S2

Extended Materials and Methods

Protein expression and purification

Human CaS receptor (UniProt (https://www.uniprot.org) code P41180-1) was cloned into a modified pEG BacMam vector (69) for expression in baculovirus-infected mammalian cells. We predicted the TM domain boundary of CaS receptor based on its homology to mGlu receptors and the known crystal structures of mGu_1 and $mGlu_5$ TM domains (62, 63). Following these predictions, we truncated the cytoplasmic tail of CaS receptor to remove flexible regions. Our expression construct contained CaS residues 1-870, where residues 1-19 belong to a signal peptide. We also engineered a Flag tag at the C-terminus to facilitate affinity purification.

Recombinant CaS receptor was produced in human embryonic kidney (HEK) 293 $GnTI^-$ cells (64) that were grown in suspension at 37°C using 293 freestyle media (Life Technologies). After infection with baculovirus carrying the CaS gene, the cells were supplemented with 10 mM sodium butyrate to improve expression level and incubated at 30°C for 72 hours before harvest. The cells were lysed using an EmulsiFlex-C3 high pressure homogenizer (Avestin) in a buffer containing 50 mM HEPES, pH 7.5, 150 mM NaCl, 10% glycerol and a cocktail of protease inhibitors (Roche). Cell debris was pelleted by centrifugation at 10,000 rpm, and the cell membrane was collected from the supernatant by ultracentrifugation at 45,000 rpm.

To purify an active form of the CaS receptor, we extracted the protein from the cell membrane with 50 mM HEPES, pH 7.5, 150 mM NaCl, 10% glycerol, 10 mM $CaCl_2$, 20 μM cyclomethyltryptophan ((3S)-2,3,4,9-tetrahydro-1H-pyrido[3,4-b]indole-3-carboxylic acid, abbreviated as TNCA), 20 μM NPS R-568 (abbreviated as R-568, 3-(2-chlorophenyl)-*N*-[(1*R*)-1-(3-methoxyphenyl)ethyl]-propan-1-amine) hydrochloride, 1% lauryl maltose neopentyl glycol (LMNG) (Anatrace), and 0.2% cholesteryl hemisuccinate (CHS) (MilliporeSigma) at 4ºC for 3 hours.

The extracted receptor was first purified by anti-Flag M2 antibody affinity chromatography. After the detergent concentration was gradually decreased to 0.002% LMNG through repeated washing, the CaS protein was eluted with 50 mM HEPES, pH 7.5, 50 mM NaCl, 10% glycerol, 10 mM $CaCl_2$, 20 μM TNCA, 20 μM R-568 hydrochloride, 0.002% LMNG, 0.0004% CHS, and 0.2 mg ml^{-1} Flag peptide. The CaS receptor was then applied to a Mono Q (GE Healthcare) ion exchange column and eluted using a linear salt gradient from 50 mM to 1 M NaCl in 50 mM HEPES, pH 7.5, 10 mM $CaCl_2$, 20 μM TNCA, 20 μM R-568 hydrochloride, 0.002% LMNG, and 0.0004% CHS. Finally, the receptor was subjected to two rounds of size exclusion chromatography using a Superose 6 Increase column (GE Healthcare). The buffer for the first size exclusion step consisted of 50 mM HEPES, pH 7.5, 100 mM NaCl, 10 mM $CaCl_2$, 30 μM TNCA, 30 μM R-568 hydrochloride, 0.005% glycol-diosgenin (GDN), and 0.00125% CHS. A similar buffer was used in the second round except the detergent concentration was increased to 0.02% GDN with 0.004% CHS.

To purify an inactive form of the CaS receptor, we extracted the protein from the cell membrane with 20 mM HEPES pH 6.8, 500 mM NaCl, 10% glycerol, 20 mM Li_2SO_4, 0.5 mM EGTA, 20 μM NPS-2143 (2-chloro-6-[(2R)-2-hydroxy-3-[(2-methyl-1-naphthalen-2-ylpropan-2-yl)amino]propoxy]benzonitrile) hydrochloride, 1% LMNG, and 0.2% CHS at 4ºC for 3 hours.

The extracted receptor was applied to an anti-Flag M2 antibody column and eluted using 20 mM HEPES pH 6.8, 100 mM NaCl, 10% glycerol, 20 mM Li_2SO_4, 20 μM NPS-2143 hydrochloride, 0.002% LMNG, 0.0004% CHS and 0.2 mg ml^{-1} Flag peptide. The following ion exchange chromatography procedure was performed using a salt gradient from 100 mM to 1 M NaCl in 20 mM HEPES pH 6.8, 20 mM Li_2SO_4, 20 μM NPS-2143 hydrochloride, 0.005% GDN,

and 0.00125% CHS. A final size exclusion chromatography step was conducted using 50 mM HEPES pH 6.8, 300 mM NaCl, 20 mM Li_2SO_4, 30 μM NPS-2143 hydrochloride, 0.02% GDN, and 0.005% CHS.

For elemental analysis, both the active and inactive-state CaS receptor were purified using LMNG detergent exclusively. For each protein sample, the purification procedure involved four chromatography steps, anti-Flag M2 antibody affinity, MonoQ ion exchange, and two consecutive rounds of Superose 6 size exclusion chromatography. To ensure accurate measurement of the elements present in the protein samples, no function-related ligand such as Ca^{2+} was added to the purification buffer in the final size exclusion procedure. Specifically, the final size exclusion buffer for active CaS receptor contained 50 mM HEPES, pH 7.5, 100 mM NaCl, 0.002% LMNG, and 0.0004% CHS, and a similar buffer was used for inactive receptor except that the pH was lowered to 6.8.

Cryo-EM specimen preparation and data acquisition

Both active- and inactive-state CaS receptor specimens were prepared using UltraAuFoil R 0.6/1, 300-mesh holey Au/Au grids (Quantifoil Micro Tools). Grid surfaces were hydrophilized with a Solarus 950 plasma cleaner system (Gatan) for 25 seconds in H_2 and O_2 at 10 watts. Vitrification was performed using a Vitrobot Mark IV (Thermo Fisher Scientific), but the experimental conditions differed slightly between functional states. For active-state CaS receptor specimens, 3 ul of purified protein was applied to charged grid surfaces at a concentration of 2.6 mg ml^{-1}. The grids were blotted for 4 or 8 seconds at a blot force of 3, and then plunge-frozen in liquid ethane. For inactive-state CaS receptor, 3 ul of protein at a concentration of 1.96 mg ml^{-1} was also blotted on grids using a blot force of 3, but for 6-8 seconds and with ashless filter paper to avoid introducing Ca^{2+} to the protein. Inactive-state CaS specimens were similarly flash cooled with liquid ethane.

Two data collections, one for each state, were performed on a Titan Krios transmission electron microscope (Thermo Fisher Scientific) equipped with a K3 direct electron detection camera (Gatan) in counting mode and a post-column GIF Quantum energy filter (Gatan) in zero-energy-loss mode with a slit width of 20 eV. All micrographs were acquired at a calibrated pixel size of 0.826 Å with a dose rate of 16 electrons per pixel per second. A nominal defocus of -1 to -2.5 μm was used for both collections. Active-state micrographs consisted of 60 frames each, collected over a 3-s exposure and resulting in a total dose of roughly 70 electrons per $Å^2$. Inactive-state micrographs each had 50 frames over a 2.5-s exposure, totaling almost 59 electrons per $Å^2$. At these respective settings, a total of 13,246 active-state and 15,464 inactive-state micrographs were acquired as dose-fractionated image stacks.

Cryo-EM image processing

The active-state dataset was imported within CryoSPARC 2.16 (65), where preliminary processing took place. The patch motion correction module was used to conduct frame alignment and dose-weighting of the raw image stacks. Estimation of contrast transfer function (CTF) for each non-dose-weighted micrograph was determined by patch CTF estimation. Meanwhile, the deep picker module incorporated within CryoSPARC was trained with a set of particles chosen from a smaller dataset that was previously acquired and processed. After scrutinizing the initial 13,246 micrographs according to CTF estimation results and degree of crystalline ice prevalence, 7,941 candidates were selected for further processing. Deep picking on this image set produced 892,000 particles, which were then extracted at a 4x binned pixel size of 3.304 Å. 2D classification

on this particle set resulted in classes representing 480,000 good particles. An *ab initio* reconstruction was generated from this set.

Heterogenous refinement was performed on four copies of the *ab initio* reconstruction, and 360,486 particles from the two most promising classes were combined and re-extracted at full scale. With one of the output classes from heterogenous refinement serving as an initial model, the combined particles were used in non-uniform refinement and yielded a 2.8 Å reconstruction. Afterwards, global CTF refinement corrected for beam tilt, spherical aberration, and higher order aberrations. Until this point, all 3D processing utilized C1 symmetry. Since the overall reconstruction displayed two-fold symmetry in both the ECD and TM domains, these particles were then used for a second round of non-uniform refinement with C2 symmetry imposed, producing a 2.6 Å reconstruction. Per-particle defocus refinement was then performed before another C2-imposed non-uniform refinement reached 2.4 Å resolution, this time including refinement of per-particle scale factors. While the ECD density map showed high resolution features at this stage, the TM domain lacked density for most side chains.

To improve the density in the TM region, the set of 360,486 particles was subjected to symmetry expansion in CryoSPARC 3.0, which duplicated the original particle poses around the C2 symmetry axis of the global reconstruction. The symmetry-expanded particle set contained the original particles as well as their symmetry mates. As a result, the total particle count doubled. The TM domain of a single CaS subunit was refined against the symmetry-expanded particle set. We then performed 3D classification of the single TM reconstruction in Relion 3.1 (66) using a mask that focused on the PAM-binding region. We obtained two main classes, corresponding to the PAM-bound and PAM-free active conformations, respectively.

The PAM-bound class contains 130,000 particles, and the corresponding single TM reconstruction was refined to 3.4 Å. Symmetry expansion was then reversed for this particle set, and the de-duplicated particles were used to calculate an overall reconstruction with C1 symmetry, which once more showed two-fold symmetry in both the ECD and TM regions. We then proceeded to generate a 2.7 Å reconstruction for the entire receptor imposing C2 symmetry. The resolution of this global reconstruction is lower than that of the full particle set (2.4 Å) due to the reduced particle number. To further improve the density, we also performed density modification of each map in Phenix (68) using the resolve_cryo_em routine. Finally, we established a composite reconstruction for the PAM-bound class by aligning two copies of the 3.4 Å individual TM map onto the 2.7 Å overall receptor reconstruction. The maximum values pointwise from the component reconstructions (*vop maximum* command in UCSF Chimera (70)) were used to generate the composite density map.

The PAM-free class consists of 105,000 particles. We conducted local refinement of a single TM domain to 3.5 Å. After reversal of symmetry expansion, we confirmed that the global reconstruction showed two-fold symmetry in the ECD and TM domains without imposing symmetry. We then obtained an overall reconstruction that reached 2.7 Å with C2 symmetry using the de-duplicated particle set. We generated a composite global reconstruction in UCSF Chimera (70) by superimposing the 2.7 Å overall reconstruction with two copies of the 3.5 Å single TM maps and taking the maximum density values at all overlapping positions.

The inactive-state image stacks were processed within CryoSPARC 3.0. As with the active state, patch motion correction and patch CTF estimation were used to align frames and estimate micrograph CTF values, respectively. From 15,464 collected micrographs, 9,524 were selected for template-based particle picking, which yielded an initial set of 1,241,782 particles. The 2D templates used in picking were generated from a subset of the selected micrographs. After the

particles were extracted with a 4x binned pixel size of 3.304 Å, additional 2D classification was performed to remove inadequate classes until 256,317 particles remained. An *ab initio* reconstruction as well as five random decoy reconstructions were produced and used for heterogenous refinement with C1 symmetry. One promising 3D class retained 161,574 particles and reached 8.0 Å resolution. Already displaying two-fold symmetry, particles from this reconstruction were extracted with 2x binning at 1.652 Å pixel size before application in a non-uniform refinement with C2 symmetry, and the resulting map reached 6.4 Å resolution. Particles were then extracted at full scale and subjected to another round of non-uniform refinement. This refinement step also imposed C2 symmetry and yielded a 5.9 Å global reconstruction.

At this stage, the full-scale particles underwent a C2 symmetry expansion, doubling the total particle count to 323,148. The individual ECD and TM domains of a CaS subunit were separately subjected to local refinement against the symmetry-expanded particle set, yielding reconstructions that reached 4.0 Å and 4.2 Å resolution, respectively. To sharpen the maps, density modification of each locally refined reconstruction was carried out in Phenix (68) using the resolve_cryo_em routine. A composite map was assembled in UCSF Chimera (70) by aligning two copies each of the ECD and TM reconstructions to the global map.

The resolution of each reconstruction was determined by the accepted 0.143 gold standard cut-off value in half-map Fourier shell correlation (FSC) curves (71, 72).

We carried out 3D variability analysis for the active-state dataset in CryoSPARC 3 (65, 73). The 360,486 particles from our C1 reconstruction were used to calculate the entire range of motions. Multiple modes of variability were observed, each represented by an eigenvector reflecting a specific aspect of conformational flexibility. The flexibility along each dimension of motion was visualized by five 3D reconstructions occupying separate stages of motion along the eigenvector, each filtered to a resolution of 4.5 Å. Transition between successive reconstructions were recorded in Chimera (70).

Model building and refinement

Construction of molecular models was carried out in Coot (67). For the PAM-bound active-state cryo-EM reconstruction, subunits from the active crystal structure of human CaS receptor ECD (PDB code: 5K5S) were positioned as rigid bodies within the extracellular portion of the receptor. This initial model was then modified to improve the fit with the surrounding density. De novo tracing was incorporated to build the linker and TM domain. The final model contained residues 21-123, 135-360, 392-703 and 722-861 for each subunit.

We also modeled one endogenous agonist TNCA, four Ca^{2+}, and one PO_4^{3-} in the ECD of each subunit. Furthermore, density at five separate N-linked glycosylation sites (Asn261, Asn287, Asn468, Asn488 and Asn541), allowed for the placement of seven N-glucosamine residues on the ECD of each subunit. Finally, density for eight molecules of either CHS or cholesterol were located between TM domains of the receptor. These densities are better fit by cholesterols than CHS molecules based on their length. Nevertheless, CHS is still a possibility if moieties are indeed disordered. We fit one PAM molecule, R-568, within the TM domain of each subunit. Refinement and validation of the fully assembled PAM-bound active structure was conducted in Phenix using real-space refinement and comprehensive validation modules, respectively (68). MolProbity was employed to determine Ramachandran statistics and non-bonded contacts of the final model (74).

The model for the PAM-bound reconstruction was fit into the PAM-free composite map with minor adjustments. The composition of the PAM-free active structure was the same as that of the PAM-bound reconstruction with two exceptions. First, only three of the N-linked

glycosylated sites (Asn468, Asn488 and Asn541) have attached carbohydrates, and a total of five N-glucosamine residues were modeled. Second, no modulator was built. The PAM-free structure was also refined and validated in Phenix (68).

For the inactive-state cryo-EM reconstruction, we used the PAM-bound active-state cryo-EM structure as the initial model. Individual domains of each subunit were separately placed into density as rigid bodies. Due to the moderate resolution of the density map, we used NAMDinator to run a molecular dynamics flexible fitting simulation for geometric optimization (46). The model was further adjusted in Coot (67) to optimize the fit to density. The final structure contained residues 21-360, 392-704 and 722-861 for each subunit. In addition, a NAM molecule, NPS-2143, was fit within the TM domain of each subunit. The model was then subjected to real-space refinement in Phenix (68). Ramachandran statistics was determined using MolProbity (74).

Pairwise structural alignment was conducted in LSQMAN (75). Figures were created using Pymol Molecular Graphics System Version 2.3 (Schrödinger), UCSF Chimera (70) and UCSF ChimeraX (76). Software support was provided by SBGrid (77).

Cell surface expression

Full-length human CaS receptor was cloned into a pcDNA3.1(+) vector (Life Technologies) for expression in HEK293 T/17 cells (ATCC). A Flag tag was inserted after the signal peptide for detection of receptors that are presented on the cell surface. Mutants of CaS receptor were constructed using the QuikChange mutagenesis system (Agilent Technologies).

The cell surface expression levels of wild-type (WT) and mutant CaS receptor were measured as previously described (78). Briefly, HEK293 T/17 cells were transfected with the CaS plasmid using Lipofectamine 3000 (Life Technologies) and cultured for one day. The cells were labeled with mouse anti-Flag M1 primary antibody (MilliporeSigma), followed by donkey anti-mouse IRDye 800-labeled secondary antibody (Li-Cor Biosciences). Fluorescent signals were captured by an Odyssey Infrared Imager (Li-Cor Biosciences). Each experiment was performed in triplicates. The amount of surface CaS protein was normalized by the cell count in each experiment. The cell surface expression level of each mutant was calculated as a percentage of the wild-type receptor.

Inositol phosphate measurement

Inositol phosphate (IP) accumulation in wild-type or mutant CaS receptor-transfected cells was quantified using the homogenous time-resolved fluorescence (HTRF) IP-one Terbium (Tb) kit (Cisbio Bioassays) as previously described (11). Varying concentrations of Ca^{2+} were deployed to induce receptor-mediated activation of endogenous G_q and its downstream signaling through inositol 1,4,5-triphosphate (IP_3). As IP_3 converts to inositol 1-monophosphate (IP_1), this accumulation was measured by competition for Tb Cryptate-coupled anti-IP_1 antibodies (donor) against a d2-labeled IP_1 analog (acceptor). Fluorescence resonance energy transfer (FRET) readings were inversely proportional to IP_1 buildup and receptor activation. The mutant receptor response was calculated as a percentage of the maximum wild-type receptor activity. The non-linear regression algorithms in Prism (GraphPad Software) was used for data analysis. Data points represent average ± s.e.m. of at least three independent experiments, each consisting of triplicate measurements.

Inductively coupled plasma mass spectrometry

Purified active (196 µl, 12.4 µg μL^{-1} or 64.0 µM) and inactive (193 µl, 15.4 µg μL^{-1} or 79.1 µM) CaS receptor samples were subjected to elemental analysis by inductively coupled plasma spectrometry (ICP-MS) following a previously described protocol (55). Briefly, each protein was digested in concentrated nitric acid ($HNO_{3)}$ (Fisher; Optima grade) and diluted with deionized water supplemented with 500 µg l^{-1} of gold (Au), as well as 5 µg L^{-1} each of gallium (Ga), iridium (Ir) and rhodium (Rh) as internal standards. The protein purification buffer containing 50 mM HEPES, pH 7.5 (active) or 6.8 (inactive), 100 mM NaCl, 0.002% LMNG, and 0.0004% CHS, was similarly digested and used as controls.

ICP-MS was conducted using a NexION 350S instrument (Perkin Elmer). The concentrations of magnesium (Mg), aluminum (Al), calcium (Ca), manganese (Mn), iron (Fe), cobalt (Co), nickel (Ni), copper (Cu), zinc (Zn), strontium (Sr), lead (Pb), cadmium (Cd) and barium (Ba) in the digested protein and buffer samples were measured. Two experiments were performed yielding eight measurements. Data points represent average ± c.v., where c.v. corresponds to coefficient of variance.

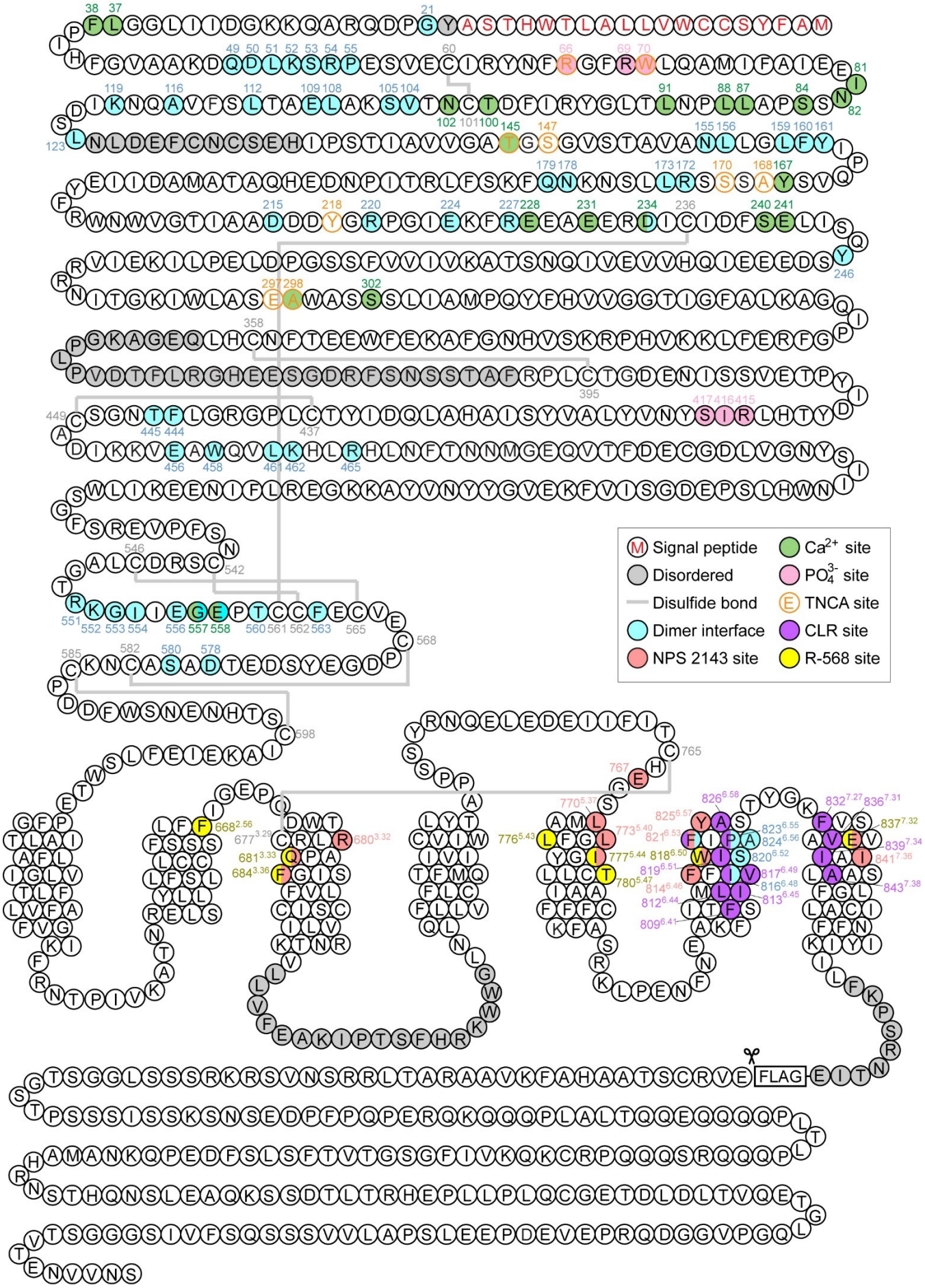
Signal peptide
Disordered
Disulfide bond
Dimer interface
NPS 2143 site
Ca2+ site
PO43- site
TNCA site
CLR site
R-568 site
FLAG

Fig. S1. Schematic diagram of the human CaS receptor.
Protein sequence of human CaS receptor, with key residues marked. Black scissors represent the position where the construct was truncated, with inserted Flag tag preceding it. Signal peptide residues are designated with red lettering, while disulfide bonds are represented by gray-colored bold lines. Other distinctions include residues that are disordered (gray), TNCA-binding (orange lettering), Ca^{2+}-binding (green), PO_4^{3-}-binding (pink), R-568-binding (yellow), NPS-2143-binding (salmon), and forming contacts at the homodimer interface directly (cyan) or through CLR (purple). TM residues incorporate a modified Ballesteros-Weinstein numbering system for class C GPCRs (79, 80).

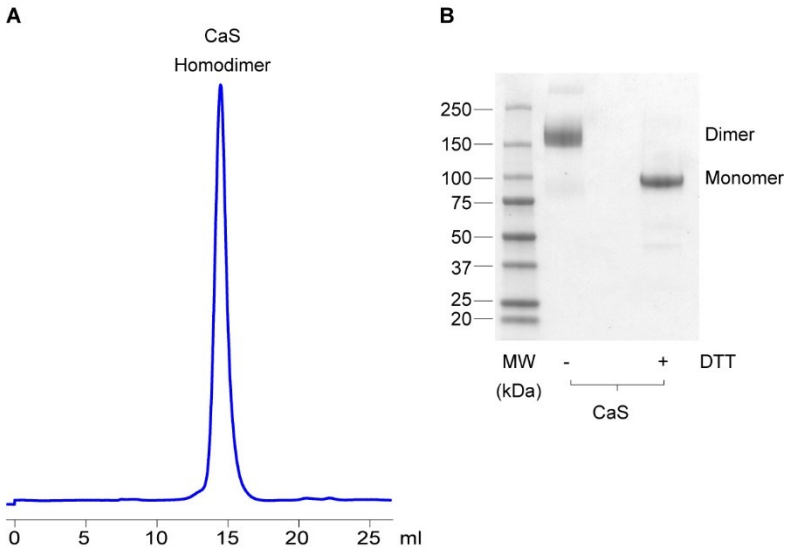

Fig. S2. Purification of human CaS receptor.
(**A**) Size exclusion chromatography profile of active-state CaS homodimer in GDN micelles.
(**B**) SDS-PAGE of purified CaS receptor under reducing and non-reducing conditions. The CaS receptor is a disulfide-linked homodimer that is reduced to monomers in the presence of the reducing reagent dithiothreitol (DTT).

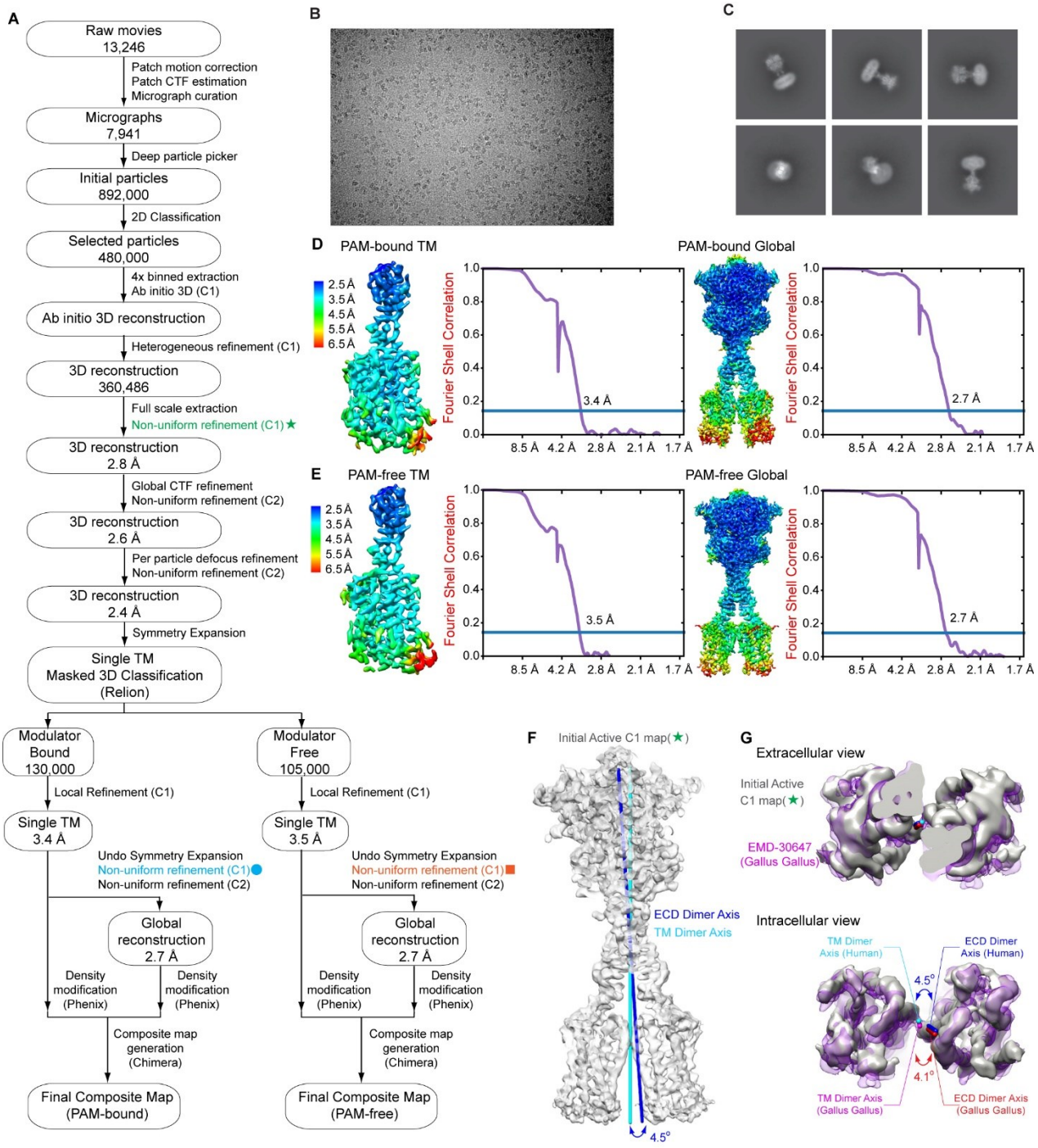
A
Raw movies
13,246
Patch motion correction
Patch CTF estimation
Micrograph curation
Micrographs
7,941
Deep particle picker
Initial particles
892,000
2D Classification
Selected particles
480,000
4x binned extraction
Ab initio 3D (C1)
Ab initio 3D reconstruction
Heterogeneous refinement (C1)
3D reconstruction
360,486
Full scale extraction
Non-uniform refinement (C1)★
3D reconstruction
2.8 Å
Global CTF refinement
Non-uniform refinement (C2)
3D reconstruction
2.6 Å
Per particle defocus refinement
Non-uniform refinement (C2)
3D reconstruction
2.4 Å
Symmetry Expansion
Single TM
Masked 3D Classification
(Relion)
Modulator
Bound
130,000
Local Refinement (C1)
Single TM
3.4 Å
Undo Symmetry Expansion
Non-uniform refinement (C1)●
Non-uniform refinement (C2)
Global
reconstruction
2.7 Å
Density
modification
(Phenix)
Density
modification
(Phenix)
Composite map
generation
(Chimera)
Final Composite Map
(PAM-bound)
Modulator
Free
105,000
Local Refinement (C1)
Single TM
3.5 Å
Undo Symmetry Expansion
Non-uniform refinement (C1)■
Non-uniform refinement (C2)
Global
reconstruction
2.7 Å
Density
modification
(Phenix)
Density
modification
(Phenix)
Composite map
generation
(Chimera)
Final Composite Map
(PAM-free)
B
C
D
PAM-bound TM
2.5 Å
3.5 Å
4.5 Å
5.5 Å
6.5 Å
PAM-bound Global
Fourier Shell Correlation
3.4 Å
2.7 Å
8.5 Å 4.2 Å 2.8 Å 2.1 Å 1.7 Å
E
PAM-free TM
PAM-free Global
3.5 Å
2.7 Å
F
Initial Active C1 map(★)
ECD Dimer Axis
TM Dimer Axis
4.5°
G
Extracellular view
Initial Active
C1 map(★)
EMD-30647
(Gallus Gallus)
Intracellular view
TM Dimer
Axis (Human)
ECD Dimer
Axis (Human)
4.5°
4.1°
TM Dimer Axis
(Gallus Gallus)
ECD Dimer Axis
(Gallus Gallus)
H
Initial Active C1★
Cinacalcet-bound
90°
I
PAM-bound C1 ●
Cinacalcet-bound
90°
J
PAM-free C1 ■
Cinacalcet-bound
90°

Fig. S3. Cryo-EM imaging of active-state CaS receptor.
(**A**) Workflow of cryo-EM data processing.
(**B**) A representative motion-corrected cryo-electron micrograph.
(**C**) A selection of reference-free 2D class averages.
(**D, E**) Density maps of PAM-bound (**D**) and PAM-free (**E**) active CaS receptor colored by local resolution (left panel) and corresponding FSC curves (purple) corrected by high-resolution noise substitution (right panel). The global map is centered on the LB2-CR homodimer interface. The single TM reconstruction is oriented 90° from the global map so that it is viewed along the TM dimer plane. Resolution of each reconstruction was determined by an FSC cut-off value of 0.143 (blue line).
(**F**) Initial active-state CaS reconstruction obtained under C1 symmetry showing the dimer axes of ECD and TM domains as well as their intersection angle (4.5°).
(**G**) Comparison of the evocalcet-bound active *Gallus gallus* CaS map (EMD-30647) (27) with our active-state C1 reconstruction. The two maps are aligned based on the ECD of one subunit. The TM dimer are viewed from the extracellular and intracellular ends. The offset of the ECD and TM dimer axes in *Gallus gallus* CaS receptor is 4.1°.
(**H-J**) Comparison of the asymmetric cinacalcet-bound active CaS map (EMD-23653) (33) with symmetric active-state CaS reconstructions generated under C1 symmetry from this study, including the initial global reconstruction (**H**), overall reconstruction for the PAM-bound (**I**) and PAM-free (**J**) classes using particle sets obtained after symmetry expansion reversal. All maps were subject to Gaussian filtering with a width of 2 Å to emphasize the overall helix shape and position. Pairwise alignment was based on the TM domain of one subunit to show two-fold symmetry in the active CaS reconstructions obtained without imposing symmetry in this study.

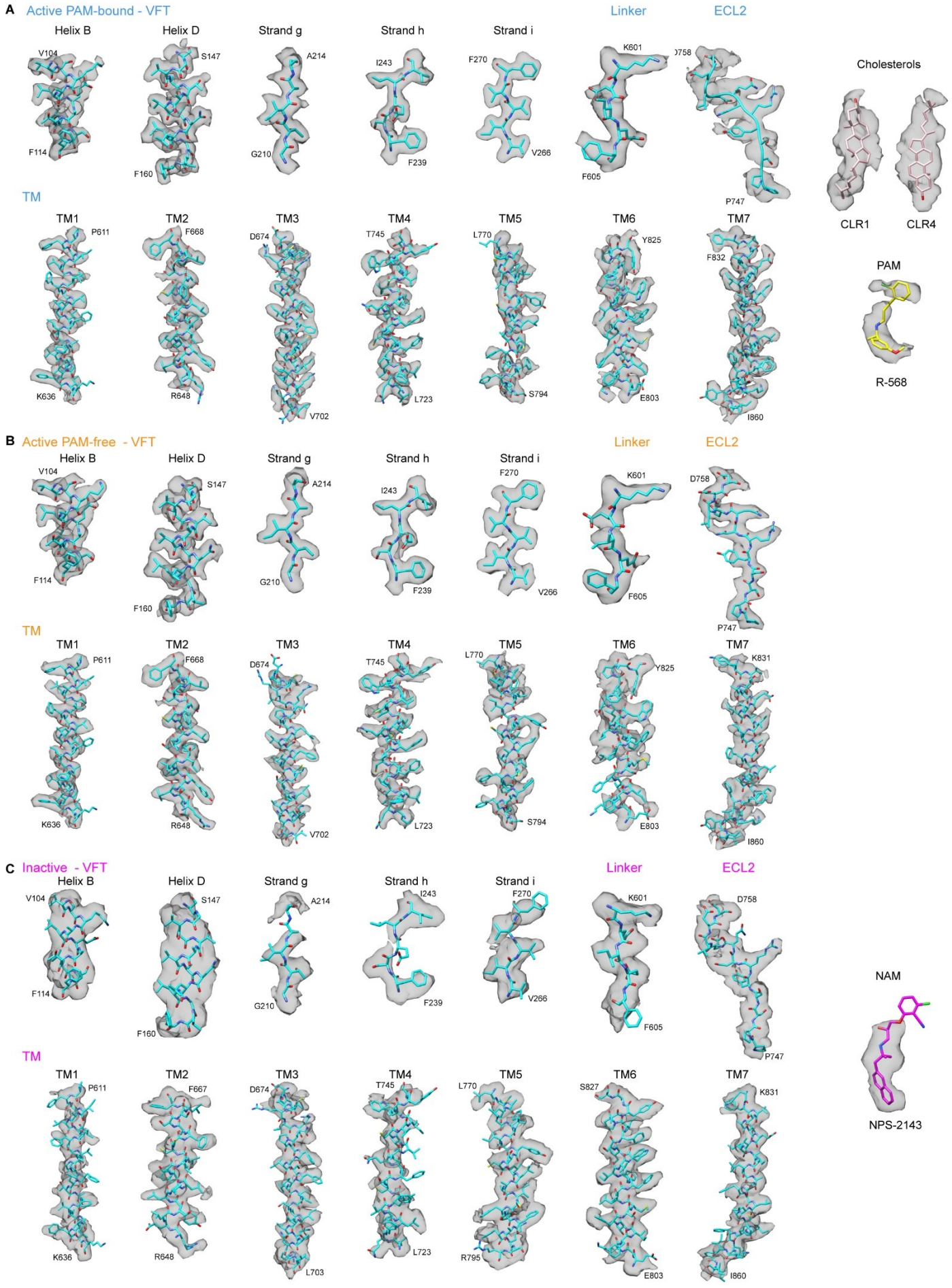
A
Active PAM-bound - VFT
Helix B
Helix D
Strand g
Strand h
Strand i
Linker
ECL2
V104
F114
S147
F160
A214
G210
I243
F239
F270
V266
K601
F605
D758
P747
Cholesterols
CLR1
CLR4
TM
TM1
TM2
TM3
TM4
TM5
TM6
TM7
P611
K636
F668
R648
D674
V702
T745
L723
L770
S794
Y825
E803
F832
I860
PAM
R-568
B
Active PAM-free - VFT
K831
C
Inactive - VFT
F667
L703
R795
S827
NAM
NPS-2143

Fig. S4. Structural models of CaS receptor fit within the cryo-EM maps.
(**A**) Structural elements of the PAM-bound active CaS receptor. Cryo-EM density maps are overlaid with corresponding parts of the refined model (hide-dust level 5). Displayed elements include those in the extracellular VFT (helices H–B and H–D at the LB1-LB1 interface; strands S–g, S-h and S-i in the LB2 domain), the linker and ECL2, all seven TM helices, the two cholesterol molecules at the dimer interface (CLR1 and CLR4), and the PAM R-568. The N- and C-termini of each helix and strand are labeled.
(**B**) Cryo-EM density map and refined model of PAM-free active CaS receptor for the same elements as those shown in (**A**) of the PAM-bound state (hide-dust level 5). No modulator density was found.
(**C**) Cryo-EM density map and refined model of inactive CaS receptor for the same structural elements as those shown in (**A**) for the active receptor (hide-dust level 5). The density for the NAM NPS-2143 is shown.

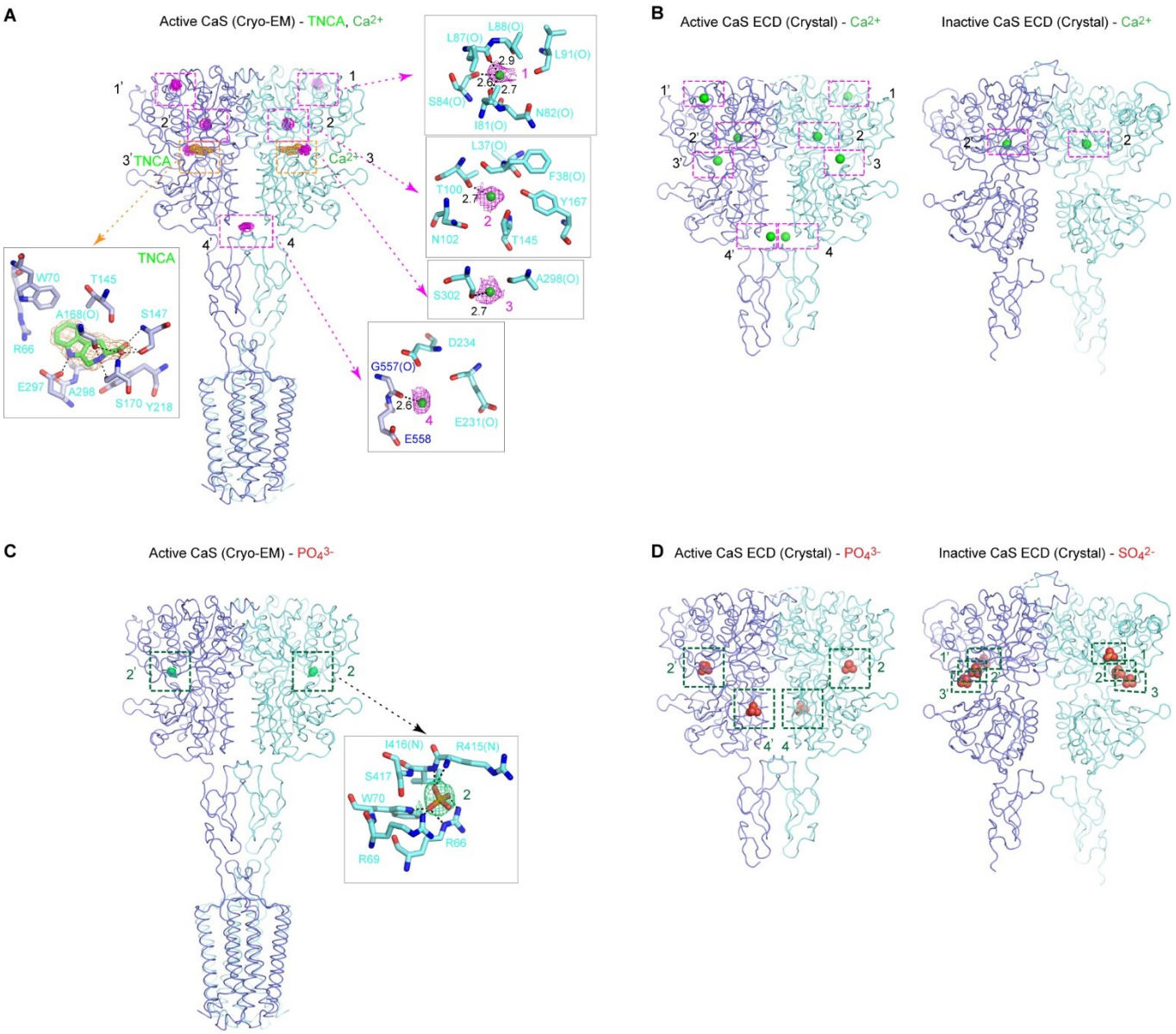

Fig. S5. Extracellular ligand binding in CaS receptor.

(**A, B**) Active-state CaS receptor showing density corresponding to bound TNCA (orange mesh; 5σ contour; 2 Å carve) and Ca^{2+} (magenta mesh; 2.5σ contour; 2 Å carve) within each subunit (**A**). Specific contacts between CaS receptor and each ligand are depicted in magnified panels (density contour for Ca^{2+}: 4σ for site 2 and 2.5σ for all other sites; 1.9-2 Å carve). Hydrogen bonds formed between the receptor and TNCA are represented by black dotted lines. Ca^{2+}-O distances within 3 Å are indicated. The locations of Ca^{2+}-binding sites 1-4 and 1'-4' are numbered following the same scheme as devised for previous crystal structures of active (PDB code 5K5S) and inactive (PDB code 5K5T) CaS receptor ECD (11) (**B**). Bound Ca^{2+} are shown as green spheres in (**B**).

(**C, D**) The same active CaS structure as presented in (**A**), with panels displaying density for PO_4^{3-} sites instead (green mesh; 5σ contour; 1.7 Å carve) (**C**). Hydrogen bonds are represented by black dotted lines. The anion site in the cryo-EM structure is numbered according to the scheme devised for the ECD crystal structures (**D**). Bound anions are shown as spheres in (**D**).

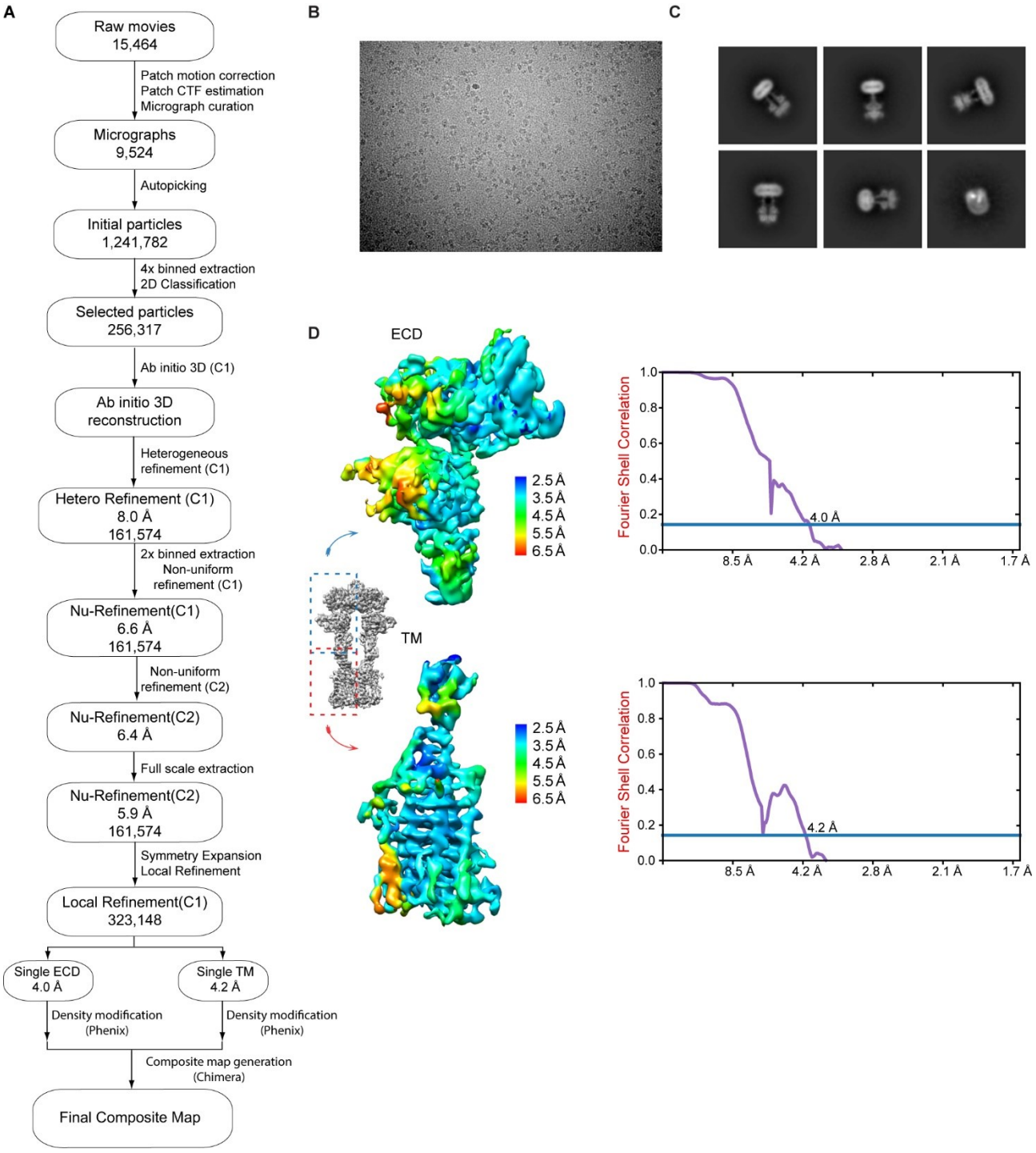

Fig. S6. Cryo-EM imaging of inactive-state CaS.
(**A**) Workflow of cryo-EM data processing.
(**B**) A representative motion-corrected cryo-electron micrograph.
(**C**) A selection of reference-free 2D class averages.
(**D**) Density maps of inactive CaS receptor colored by local resolution (left panel) and corresponding FSC curves (purple) corrected by high-resolution noise substitution (right panel). The single ECD and TM reconstructions are viewed along the LB2-CR and TM dimer planes. The resolution of each reconstruction was determined by an FSC cut-off value of 0.143 (blue line).

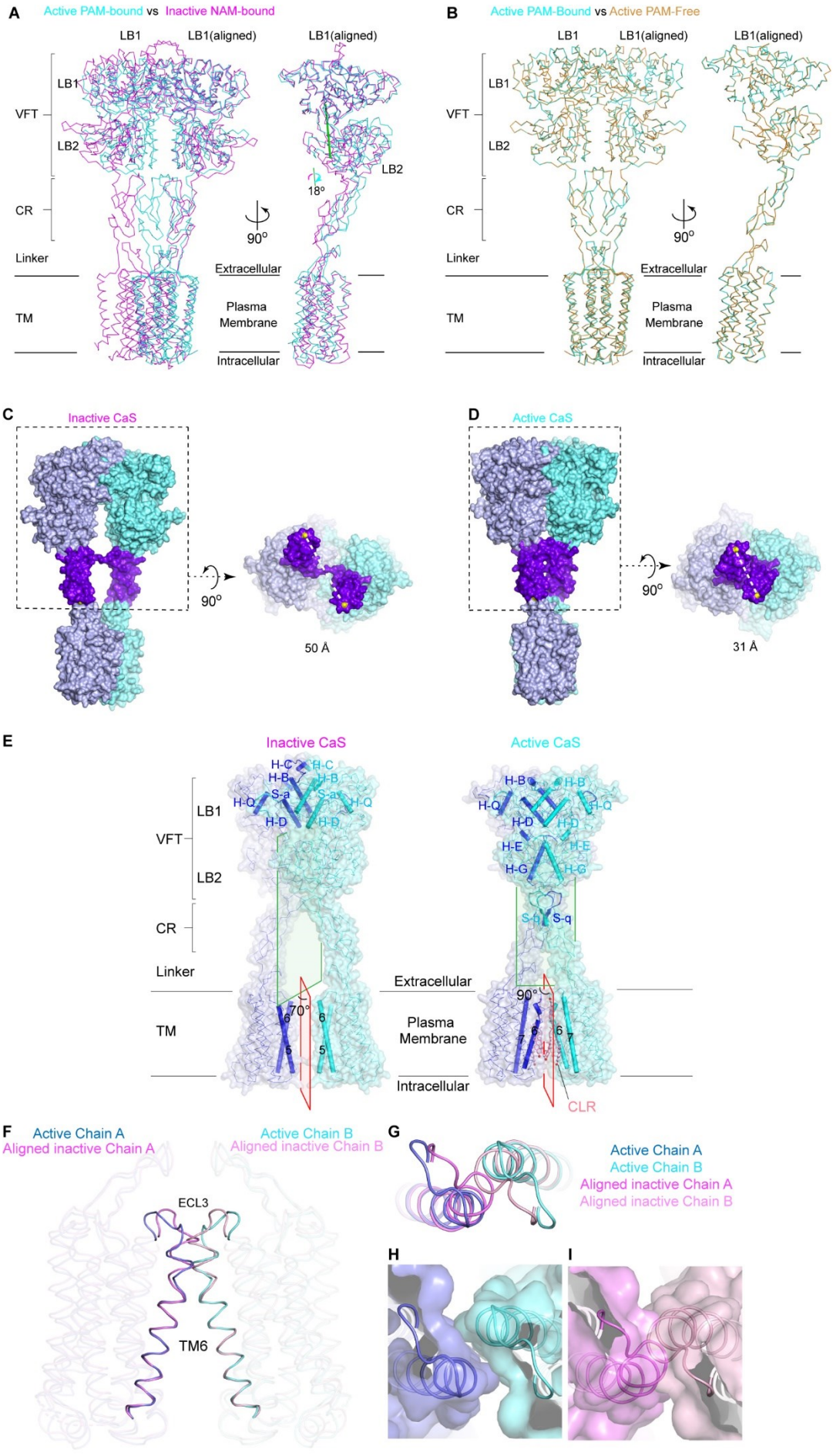
A
Active PAM-bound vs Inactive NAM-bound
LB1
LB1(aligned)
LB1(aligned)
VFT
LB1
LB2
CR
Linker
TM
LB2
18°
90°
Extracellular
Plasma Membrane
Intracellular
B
Active PAM-Bound vs Active PAM-Free
LB1
LB1(aligned)
LB1(aligned)
VFT
LB1
LB2
CR
Linker
TM
90°
Extracellular
Plasma Membrane
Intracellular
C
Inactive CaS
90°
50 Å
D
Active CaS
90°
31 Å
E
Inactive CaS
Active CaS
H-C
H-B
S-a
H-Q
H-D
H-E
H-G
S-q
LB1
VFT
LB2
CR
Linker
TM
Extracellular
Plasma Membrane
Intracellular
70°
90°
6
5
7
CLR
F
Active Chain A
Aligned inactive Chain A
Active Chain B
Aligned inactive Chain B
ECL3
TM6
G
Active Chain A
Active Chain B
Aligned inactive Chain A
Aligned inactive Chain B
H
I

Fig. S7. Activation-associated conformational changes.
(**A**) Superposition of the PAM-bound active (cyan) and NAM-bound inactive (magenta) structures of CaS receptor. Two orthogonal views are presented. Alignment is based on pairing the LB1 domain of one subunit. Included is the axis (green rod) and degree of rotation required to align corresponding LB2 domains of these structures.
(**B**) Superposition of the PAM-bound (cyan) and PAM-free (orange) active CaS receptor structures in two orthogonal views.
(**C, D**) Space-filling representations of inactive-state (**C**) and active-state (**D**) structures of CaS receptor. The side panel views the extracellular domain from the C-terminal ends of CR domains. The distance between the tips of the CR domains (Cα of Asp588; yellow) in each dimer is represented by a white dashed line and labeled below the diagram.
(**E**) Intersection angle between the homodimer interfacial planes of membrane-proximal LB2-CR units and TM domains in the active and inactive CaS receptor. Structural elements involved in homodimer formation are highlighted in cartoon format within each structure.
(**F-I**) Inactive TM6 conformation is incompatible with an active TM6-TM6 dimer orientation. Superposition of individual TM domains of inactive CaS receptor separately onto each subunit of the PAM-bound active structure. The alignment was based on the intracellular portion of TM6 ($A804^{6.36}$-$I816^{6.48}$). Both the side (**F**) and top views (**G**) show the clash between the extracellular end of TM6 and ECL3 of both subunits. Molecular surface representations compare the active TM dimer disposition (**H**) and the clash between inactive TM domains when aligned onto the active TM dimer (**I**).

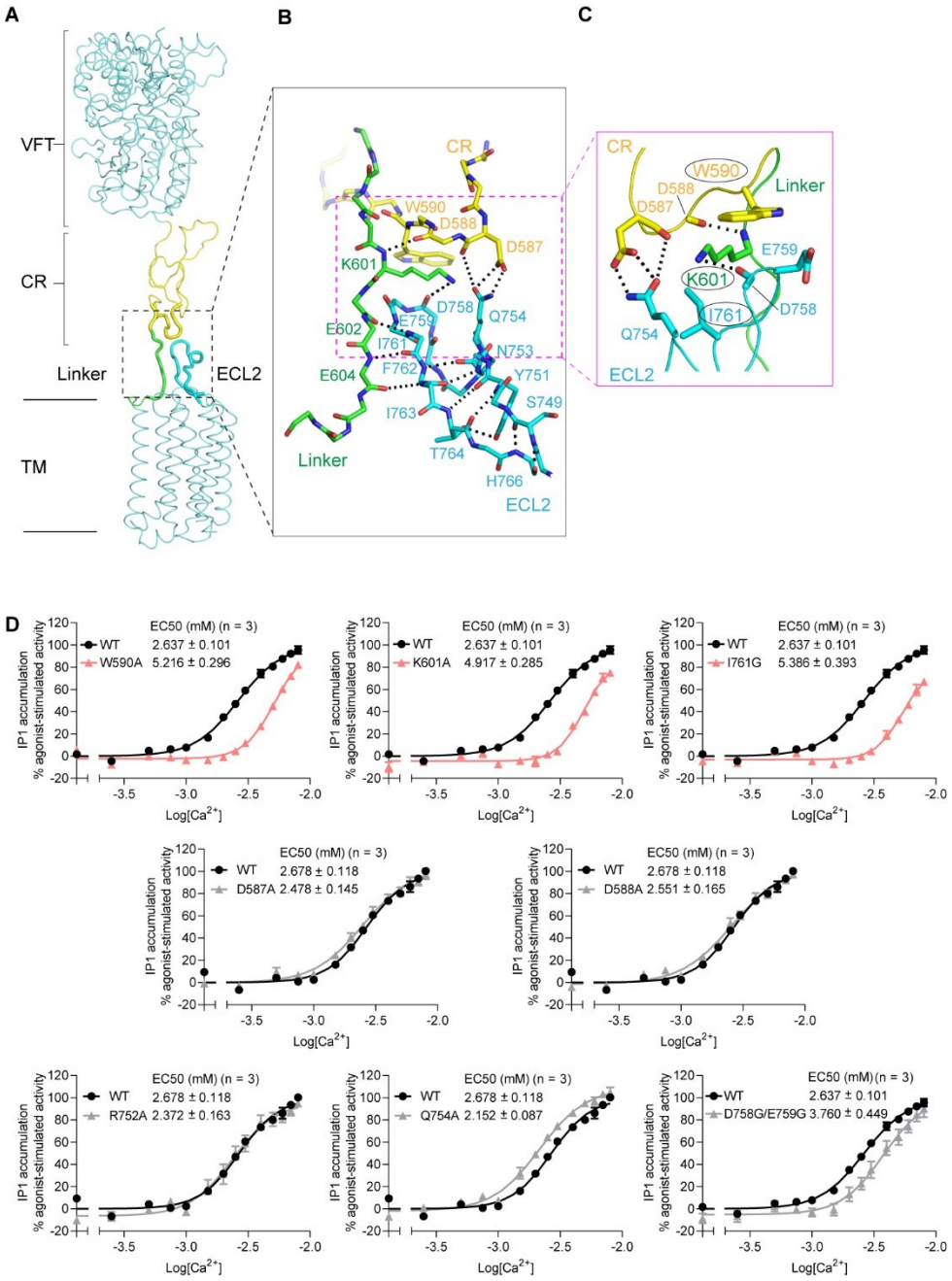

Fig. S8. Mechanical junction for communication between VFT and TM domains.
(**A**) Structure of a CaS receptor subunit highlighting the mechanical junction formed by CR (yellow), linker (green) and ECL2 (cyan).
(**B**) Detailed view of the hydrogen-bond network between linker and ECL2.
(**C**) Stacking interactions formed by key residues at the junction, including K601 (linker), W590 (CR), and I761 (ECL2).
(**D**) Functional analysis of the CR-linker-ELC2 entity. Dose-dependent Ca^{2+}-stimulated IP_1 accumulation was measured in cells transiently expressing either wild-type (WT) or mutant CaS receptor bearing one of several substitutions at the junction. Cell surface expression levels of the mutants W590A, K601A, I761G, R752A, Q754A, D758G/E759G, D587A, and D588A were 125%, 86%, 81%, 106%, 99%, 92%, 101%, and 91% of WT level, respectively. Data points represent average ± s.e.m. of three independent experiments (n=3), each with triplicate measurements.

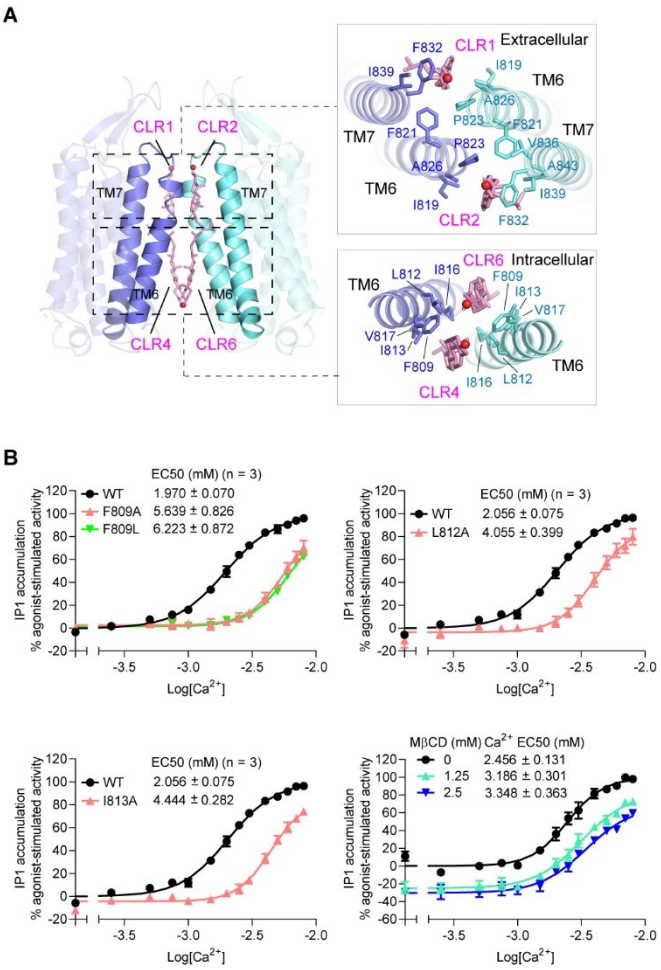

Fig. S9. Cholesterol-mediated dimer interactions in active CaS receptor.
(**A**) CLR-mediated dimer interactions in the PAM-bound active CaS receptor structure. Magnified panels show the specific contacts near the extracellular (top) and intracellular (bottom) membrane surface, respectively. The CLR-mediated dimer contacts at the extracellular end are peripheral to the direct TM6-TM6 interactions.
(**B**) Functional analysis of CLR-mediated TM dimer contacts. Ca^{2+}-dependent IP_1 accumulation was measured in cells transiently expressing either WT or mutant CaS receptor bearing one of the selected substitutions at the TM dimer interface. Cell surface expression levels of the F809A, F809L, L812A, and I813A mutants were 87%, 98%, 83%, and 87% of WT level, respectively. Data points represent average ± s.e.m. of multiple experiments (n), each with triplicate measurements. Function of CaS receptor was also assessed in the absence and presence of varying concentrations of methyl-β-cyclodextrin (1.25 and 2.5 mM).

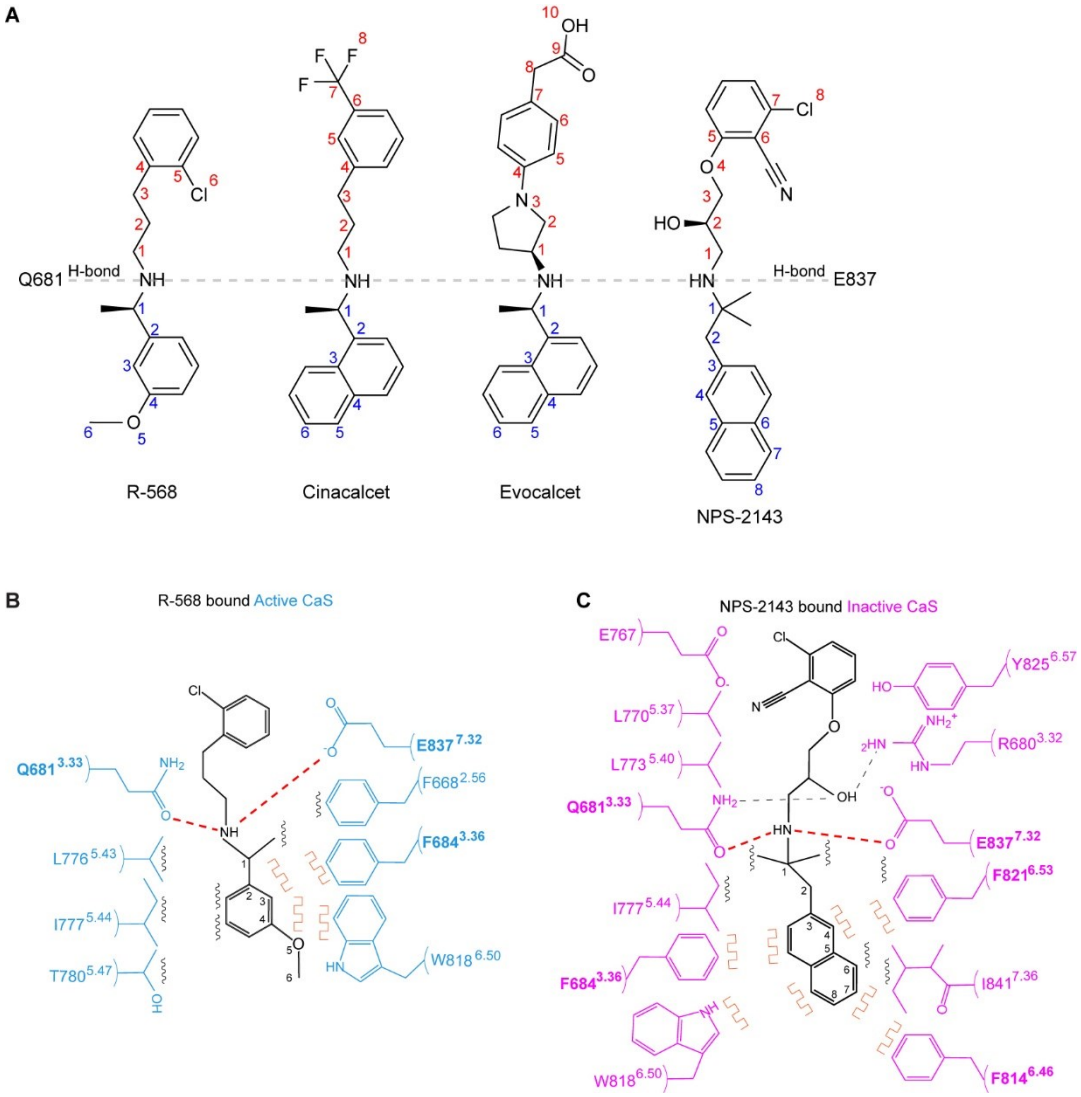

Fig. S10. Modulator binding to CaS receptor.
(**A**) Schematic diagram of various PAM (R-568, cinacalcet and evocalcet) and NAM (NPS-2143) molecules of CaS receptor.
(**B**) Schematic diagram of the specific contacts between active CaS receptor and PAM R-568.
(**C**) Schematic diagram of the specific contacts between inactive CaS receptor and NAM NPS-2143. Selected contacts are highlighted; hydrogen bonds, red dotted lines; potential hydrogen bonds, black dotted lines; hydrophobic contacts, black wiggled lines; aromatic π-stacking interactions, orange box wave. Residues surrounding the disordered chlorobenzonitrile group of NPS-2143 (E767, L770, L773, and Y825) are shown without marking any specific contact.

Table S1. Cryo-EM data collection, refinement and validation statistics

	Active CaS PAM-bound (EMD-25143) (PDB 7SIL)	Active CaS PAM-free (EMD-25144) (PDB 7SIM)	Inactive CaS NAM-bound (EMD-25145) (PDB 7SIN)
Data collection and processing			
Magnification	105,000 x	105,000 x	105,000 x
Voltage (kV)	300	300	300
Electron exposure (e–/Å^2)	70.35	70.35	58.63
Defocus range (μm)	-1 to -2.5	-1 to -2.5	-1 to -2.5
Pixel size (Å)	0.826	0.826	0.826
Symmetry imposed	C2	C2	C2
Initial particle images (no.)	892,000	892,000	1,241,782
Final particle images (no.)	130,000	105,000	161,574
Map resolution (Å) (ECD/TM)	2.7/3.4	2.7/3.5	4.0/4.2
FSC threshold	0.143	0.143	0.143
Refinement			
Initial model used (PDB code)	–	–	–
Model resolution (Å)	2.8	2.7	6.5
FSC threshold	0.5	0.5	0.5
Map sharpening *B* factor (Å^2)			
Model composition			
Non-hydrogen atoms	12,930	12,826	12,664
Protein residues	1562	1562	1585
Ligands - Ca^{2+}	8	8	–
PO_4^{3-}	2	2	–
TNCA	2	2	–
R-568	2	–	–
NPS-2143	–	–	2
CLR	8	8	–
Sugar	14	10	–
Water	–	–	–
B factors (Å^2)			
Protein	27.0	32.6	141.8
Ligands - Ca^{2+}	33.7	38.8	–
PO_4^{3-}	15.8	21.9	–
TNCA	15.6	18.9	–
R-568	29.9	–	–
NPS-2143	–	–	84.1
CLR	34.0	47.4	–
Sugar	41.1	45.8	–
Water	–	–	–
R.m.s. deviations			
Bond lengths (Å)	0.004	0.005	0.003
Bond angles (°)	0.909	0.940	0.618
Validation			
MolProbity score	1.38	1.43	1.66
Clash score	6.57	7.90	8.54
Poor rotamers (%)	0.15	0.07	0.00
Ramachandran plot			
Favored (%)	97.9	98.3	96.8
Allowed (%)	2.1	1.7	3.2
Disallowed (%)	0.0	0.0	0.0

Table S2. Elemental analysis of active and inactive CaS receptor

			Mg	Ca	Co	Ni	Zn	Cu	Sr	Ba	Pb	Al	Mn	Fe	Cd
active CaS	Buffer $[M_B]$[1]	µg/L	0.20	8.07	0.00	0.01	0.70	0.29	0.09	0.03	0.00	0.36	0.00	0.00	0.00
		C.V.[2]	2.2%	1.0%	9.5%	11.9%	1.6%	1.2%	1.3%	2.0%	21.6%	8.9%	7.1%	25.9%	26.2%
	Protein[3] $[M_P]$[1]	µg/L	0.86	44.75	0.01	0.81	41.29	9.50	0.15	0.05	0.11	1.61	0.02	4.44	0.04
		C.V.[2]	1.2%	1.3%	4.3%	1.2%	0.7%	0.8%	1.5%	1.5%	0.6%	2.1%	2.9%	0.7%	4.4%
	Net [M][1] ($[M_p]$ - $[M_B]$)	µg/L	0.66	36.68	0.01	0.80	40.59	9.21	0.05	0.02	0.11	1.25	0.02	4.45	0.04
		µM	0.03	0.92	0.00	0.01	0.62	0.14	0.00	0.00	0.00	0.05	0.00	0.08	0.00
	Ratio[4] Net [M] / [P]		0.02	0.73	0.00	0.01	0.49	0.12	0.00	0.00	0.00	0.04	0.00	0.06	0.00
			Mg	**Ca**	**Co**	**Ni**	**Zn**	**Cu**	**Sr**	**Ba**	**Pb**	**Al**	**Mn**	**Fe**	**Cd**
inactive CaS	Buffer $[M_B]$[1]	µg/L	0.11	4.22	0.00	0.00	0.21	0.05	0.16	0.01	0.00	0.25	0.00	0.14	0.00
		C.V.[2]	4.8%	2.7%	8.3%	54.9%	3.2%	3.6%	0.9%	3.5%	256.9%	2.6%	17.9%	53.5%	26.1%
	Protein[5] $[M_P]$[1]	µg/L	1.23	20.67	0.01	0.17	2.79	13.68	0.20	0.05	0.05	6.80	0.03	3.69	0.01
		C.V.[2]	0.7%	1.3%	3.3%	1.5%	1.0%	1.0%	1.0%	1.7%	1.9%	0.9%	1.7%	2.1%	10.2%
	Net [M][1] ($[M_p]$ - $[M_B]$)	µg/L	1.12	16.45	0.01	0.17	2.57	13.63	0.04	0.03	0.05	6.56	0.03	3.55	0.01
		µM	0.05	0.41	0.00	0.00	0.04	0.21	0.00	0.00	0.00	0.24	0.00	0.06	0.00
	Ratio[4] Net [M] / [P]		0.03	0.27	0.00	0.00	0.03	0.14	0.00	0.00	0.00	0.16	0.00	0.04	0.00

[1]$[M_B]$ is metal concentration in buffer; [MP] is metal concentration in active CaS protein sample; Net [M] is the metal concentration in protein sample after buffer correction.
[2]C.V. is coefficient of variance
[3]Protein concentration in active CaS homodimer sample [P] is 1.25 µM.
[4]Molar ratio of net metal concentration to protein concentration.
[5]Protein concentration in inactive CaS homodimer sample [P] is 1.53 µM.
Data represents average of two measurements within one experiment.

Movies S1 (Separate file)**.** Conformational variability analysis of PAM-bound active CaS receptor. Motion between the TM domains of the two subunits as revealed by 3D variability analysis of the entire receptor. The TM domains oscillate relative to each other.

Movies S2 (Separate file)**.** Conformational variability analysis of PAM-bound active CaS receptor. Motion between the ECD and TM domains as revealed by 3D variability analysis of the entire receptor. The ECD and TM domains flex back and forth about the linker region.

.

SI references

69. A. Goehring *et al.*, Screening and large-scale expression of membrane proteins in mammalian cells for structural studies. *Nat. Protoc.* **9**, 2574-2585 (2014).
70. E. F. Pettersen *et al.*, UCSF Chimera--a visualization system for exploratory research and analysis. *J. Comput. Chem.* **25**, 1605-1612 (2004).
71. P. B. Rosenthal, R. Henderson, Optimal determination of particle orientation, absolute hand, and contrast loss in single-particle electron cryomicroscopy. *J. Mol. Biol.* **333**, 721-745 (2003).
72. S. H. Scheres, S. Chen, Prevention of overfitting in cryo-EM structure determination. *Nat Methods* **9**, 853-854 (2012).
73. A. Punjani, D. J. Fleet, 3D variability analysis: Resolving continuous flexibility and discrete heterogeneity from single particle cryo-EM. *J. Struct. Biol.* **213**, 107702 (2021).
74. V. B. Chen *et al.*, MolProbity: all-atom structure validation for macromolecular crystallography. *Acta Crystallogr. D Biol. Crystallogr.* **66**, 12-21 (2010).
75. M. Novotny, D. Madsen, G. J. Kleywegt, Evaluation of protein fold comparison servers. *Proteins* **54**, 260-270 (2004).
76. T. D. Goddard *et al.*, UCSF ChimeraX: Meeting modern challenges in visualization and analysis. *Protein Sci.* **27**, 14-25 (2018).
77. A. Morin *et al.*, Collaboration gets the most out of software. *Elife* **2**, e01456 (2013).
78. S. Burmakina, Y. Geng, Y. Chen, Q. R. Fan, Heterodimeric coiled-coil interactions of human GABAB receptor. *Proc. Natl. Acad. Sci. U. S. A.* **111**, 6958-6963 (2014).
79. J. A. Ballesteros, H. Weinstein, Integrated Methods for the Construction of Three-Dimensional Models and Computational Probing of Structure-Function Relations in G Protein-Coupled Receptors *Methods in Neuroscience* **25**, 366-428 (1995).
80. J. P. Pin, T. Galvez, L. Prezeau, Evolution, structure, and activation mechanism of family 3/C G-protein-coupled receptors. *Pharmacol. Ther.* **98**, 325-354 (2003).